# Giant photonic spin Hall effect empowered by polarization-dependent quasibound states in the continuum in compound grating waveguide structures

Feng Wu [1,*] Tingting Liu [2,3] Yang Long [4] Shuyuan Xiao [2,3] and Gengyan Chen [1]

[1] *School of Optoelectronic Engineering, Guangdong Polytechnic Normal University, Guangzhou 510665, China*

[2] *Institute for Advanced Study, Nanchang University, Nanchang 330031, China*

[3] *Jiangxi Key Laboratory for Microscale Interdisciplinary Study, Nanchang University, Nanchang 330031, China*

[4] *Division of Physics and Applied Physics, School of Physical and Mathematical Sciences, Nanyang Technological University, Singapore 637371, Singapore*

(Received 11 January 2023; revised 18 April 2023; accepted 19 April 2023; published 27 April 2023)

The photonic spin Hall effect (PSHE) plays an important role in both fundamental science and precision metrology. In this paper, we theoretically propose a polarization-dependent bound state in the continuum (BIC) in a compound grating waveguide structure based on the selectable guided resonance at near-infrared wavelengths. Empowered by the unique resonant property and polarization-dependent property of the quasi-BIC, the transverse shift of the PSHE can be intensively enhanced to the order of hundreds of micrometers. Besides, the enhancement of the transverse shift of the PSHE is robust against the geometric parameters. Our work not only provides an all-dielectric platform to achieve giant PSHE, but also offers a viable approach to design high-performance PSHE-based optical devices.

DOI: 10.1103/PhysRevB.107.165428

## I. INTRODUCTION

As an optical analogy of the spin Hall effect in electronic systems, the photonic spin Hall effect (PSHE) has attracted rich attention over the past decades [1–4]. The PSHE refers to the displacement perpendicular to the incident plane for the splitting of left and right circularly polarized components when a linearly polarized light beam launches onto a structure [5–8]. The underlying physics of the PSHE is the spin-orbit interaction [9–11]. To date, the PSHE has been widely utilized in biosensing [12–15], layer thickness measurement [16], optical conductivity measurement [17], optical imaging [18], and optical computing [19]. The PSHE is also related to the Imbert-Fedorov effect [20–25]. The Imbert-Fedorov effect was theoretically predicted by Fedorov in 1955 [26] and experimentally verified by Imbert in 1972 [27]. In the case of total reflection, the transverse shift of the PSHE is generally on the subwavelength scale owing to the weak spin-orbit interaction [28,29]. Such tiny transverse shift poses a challenge in direct measurement in experiments. Enabled by the weak measurement technique, researchers can observe the subwavelength transverse shift of the PSHE in experiments [30–34]. To enhance the PSHE, researchers proposed various nanostructures, including metasurfaces [35–40], photonic crystals [41–44], surface plasmon resonance configurations [45,46], graphene-based nanostructures [47,48], nanoapertures [49], dielectric particle arrays [50], and hyperbolic metamaterials [51–53].

Over the past two decades, bound states in the continuum (BICs) have been widely explored due to their unique physical properties [54–57]. Different from conventional discrete bound states, BICs are embedded in the continuous spectra [54–57]. When the parameter perturbation is introduced, true BICs with infinite $Q$ factors will turn into quasi-BICs with ultrahigh $Q$ factors. To date, a series of nanostructures have been proposed to achieve quasi-BICs, including waveguides [58–60], metasurfaces [61,62], photonic crystal slabs [63–67], subwavelength gratings [68–77], and nanoparticles [78]. In 2019, Jiang *et al.* enhanced the PSHE by the quasi-BIC in an epsilon-near-zero material slab [79]. For a lossless epsilon-near-zero material slab, the transverse shift of the PSHE can be enhanced to the order of hundreds of micrometers. However, it is known that epsilon-near-zero material possesses inevitable optical loss at optical wavelengths [80]. When considering the optical loss of the epsilon-near-zero material, the transverse shift of the PSHE only reaches the order of micrometers [79]. Very recently, Wang *et al.* discovered a special PSHE (spin-related in-plane-oblique lateral beam shifts) by the quasi-BIC in a photonic crystal slab [81]. The strong spin-orbit interactions of light are induced by the topological vortex around BIC. The measured beam shift of the PSHE reaches the order of micrometers. In this paper, we theoretically propose a polarization-dependent BIC in a compound grating waveguide structure based on the selectable guided resonance at near-infrared wavelengths. Empowered by the polarization-dependent quasi-BIC, the transverse shift of the PSHE can be intensively enhanced to the order of hundreds of micrometers. Our work provides a feasible route to achieving giant PSHE and designing high-performance PSHE-based optical devices.

This paper is organized as follows. In Sec. II, we start from the guided-mode resonance (GMR) conditions in a compound grating waveguide structure composed of a four-part period

*fengwu@gpnu.edu.cn

 

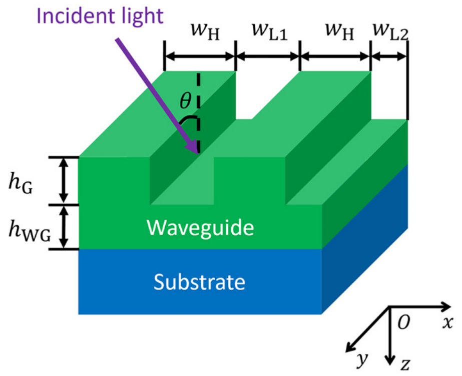


FIG. 1. Schematic of the unit cell of the compound grating waveguide structure. First layer is a four-part period grating layer with the period $\Lambda$ and the height $h_G$. First and third parts are $HfO_2$ ridges with the refractive index $n_H$, while the second and fourth parts are air grooves with the refractive index $n_L$. Widths of two $HfO_2$ ridges are set to be the same value, $w_H = f_H\Lambda = 0.3\Lambda$. Widths of two air grooves are set to be $w_{L1} = f_{L1}\Lambda$ and $w_{L2} = f_{L2}\Lambda$, respectively. Second layer is a $HfO_2$ waveguide layer with the height $h_{WG}$. Third layer is a $SiO_2$ substrate with the refractive index $n_S$. Suppose that a plane wave obliquely launches onto the structure with the incident angle $\theta = 5^\circ$. Incident plane is $xOz$ plane.

grating and a waveguide layer under *s* and *p* polarizations. When the four-part period grating reduces to a two-part period grating, the grating-induced tangential wave vector doubles. Therefore, the previous excitable odd-order guided resonance becomes unexcitable. Based on such selectable guided resonance, a BIC can be theoretically realized. Owing to the polarization-dependent property of the dispersion relation of the guided mode, the BIC is also polarization dependent. In Sec. III, we utilize the polarization-dependent quasi-BIC to enhance the PSHE. Specifically, the transverse shift of the PSHE can be intensively enhanced to the order of hundreds of micrometers. The influences of the geometric parameters on the transverse shift of the PSHE are also investigated. Finally, the conclusion is given in Sec. IV.

## II. POLARIZATION-DEPENDENT BICS IN COMPOUND GRATING WAVEGUIDE STRUCTURES

The unit cell of the compound grating waveguide structure is schematically shown in Fig. 1. The first layer is a four-part period grating layer with the period $\Lambda = 962$ nm and the height $h_G = 750$ nm. The first and third parts are hafnium dioxide ($HfO_2$) ridges with the refractive index $n_H$ while the second and fourth parts are air grooves with the refractive index $n_L = 1$. The widths of two $HfO_2$ ridges are set to be the same value, $w_H = f_H\Lambda = 0.3\Lambda$. The widths of two air grooves are set to be $w_{L1} = f_{L1}\Lambda$ and $w_{L2} = f_{L2}\Lambda$, respectively. We define a tunable geometric parameter $\Delta = (w_{L1} - w_{L2})/(w_{L1} + w_{L2})$ to reflect the width difference between two air grooves. The second layer is a $HfO_2$ waveguide layer with the height $h_{WG} = 320$ nm. To investigate the behavior of the BIC, we ignore the intrinsic and scattering losses of $HfO_2$ in Sec. II. The refractive index of $HfO_2$ is set to be $n_H = 1.88$ [82]. In Sec. III, we will consider the intrinsic and scattering losses of $HfO_2$. The third layer is a silicon dioxide ($SiO_2$) substrate with the refractive index $n_S = 1.44$ [83]. Suppose that a plane wave obliquely launches onto the structure with the incident angle $\theta = 5^\circ$. The incident plane is $xOz$ plane.

The functionality of the waveguide layer is to provide the guided mode. The functionality of the four-part period grating layer is to provide the additional tangential wave vector called the grating-induced tangential wave vector due to the discrete periodicity of the structure. Owing to the grating-induced tangential wave vector, the incident light can strongly couple with the guided mode at some specific frequencies [84]. Such phenomenon is known as the GMR [84].

When the tunable geometric parameter $\Delta \neq 0$, the widths of two air grooves are different ($w_{L1} \neq w_{L2}$). Therefore, the grating layer is a four-part period grating with the period $\Lambda$. The GMR condition is expressed as [84]

$$k_{x,m} = k_0 \sin\theta - m\frac{2\pi}{\Lambda} = \beta \ (m = \pm 1, \ \pm 2, \ldots), \quad (1)$$

where $k_0 \sin\theta = \omega \sin\theta / c$ represents the tangential wave vector of the incident light, $m \times (2\pi/\Lambda)$ represents the grating-induced tangential wave vector, and $\beta$ represents the propagating constant of the guided mode in the waveguide layer.

In the case of *s* polarization, we focus on the $TE_0$ guided mode. The dispersion relation of the $TE_0$ guided mode can be expressed as [85]

$$h_{WG}\sqrt{k_0^2 n_{WG}^2 - \beta_{TE_0}^2} = \arctan\left(\frac{\sqrt{\beta_{TE_0}^2 - k_0^2 n_0^2}}{\sqrt{k_0^2 n_{WG}^2 - \beta_{TE_0}^2}}\right) + \arctan\left(\frac{\sqrt{\beta_{TE_0}^2 - k_0^2 n_S^2}}{\sqrt{k_0^2 n_{WG}^2 - \beta_{TE_0}^2}}\right). \quad (2)$$

The dispersion relation of the $TE_0$ guided mode is shown by the black solid line in Fig. 2(a). The normalized angular frequency is set to be $\omega_0 = 2\pi c/h_{WG}$. The cutoff angular frequency of the $TE_0$ guided mode is $\omega_{c,\,TE_0} = 0.0933\omega_0$. The dispersion relations $k_{x,+1}$ and $k_{x,+2}$ are shown by the blue and red dashed lines in Fig. 2(a). Apparently there are two crossing points, which are marked by $A_{+1}$ and $A_{+2}$. The corresponding angular frequencies are $\omega_{+1} = 0.2027\omega_0$ ($\lambda_{+1} = 1578.7$ nm) and $\omega_{+2} = 0.3724\omega_0$ ($\lambda_{+2} = 859.3$ nm). At these two angular frequencies, the GMR condition is satisfied and gives rise to Fano resonances.

In the case of *p* polarization, we focus on the $TM_0$ guided mode. The dispersion relation of the $TM_0$ guided mode can be expressed as [85]

$$h_{WG}\sqrt{k_0^2 n_{WG}^2 - \beta_{TM_0}^2} = \arctan\left(\frac{n_{WG}^2\sqrt{\beta_{TM_0}^2 - k_0^2 n_0^2}}{n_0^2\sqrt{k_0^2 n_{WG}^2 - \beta_{TM_0}^2}}\right) + \arctan\left(\frac{n_{WG}^2\sqrt{\beta_{TM_0}^2 - k_0^2 n_S^2}}{n_S^2\sqrt{k_0^2 n_{WG}^2 - \beta_{TM_0}^2}}\right). \quad (3)$$

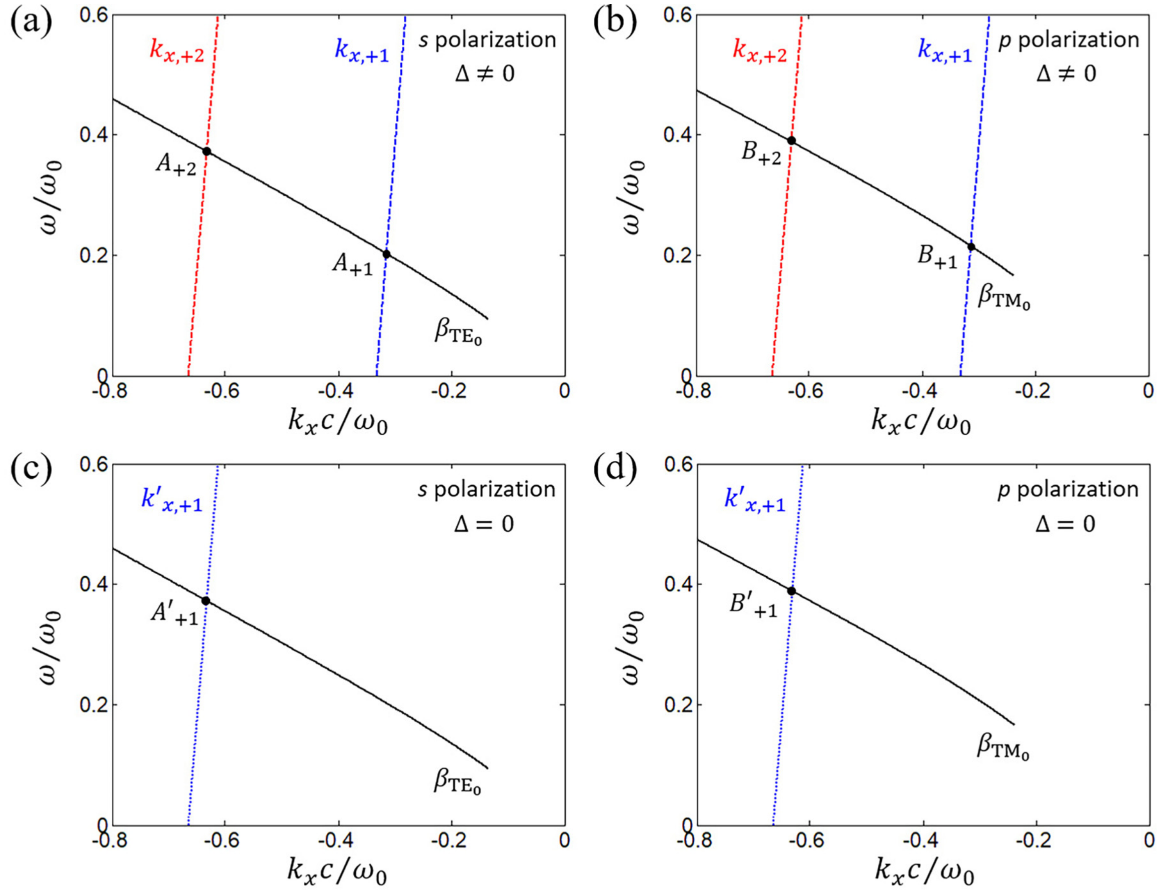


FIG. 2. (a) GMR in the compound grating waveguide structure under $s$ polarization when $\Delta \neq 0$. (b) GMR in the compound grating waveguide structure under $p$ polarization when $\Delta \neq 0$. (c) GMR in the compound grating waveguide structure under $s$ polarization when $\Delta = 0$. (d) GMR in the compound grating waveguide structure under $p$ polarization when $\Delta = 0$. Other parameters are set to be $\Lambda = 962$ nm, $h_{\mathrm{WG}} = 320$ nm, $n_{\mathrm{H}} = 1.88$, $n_{\mathrm{L}} = 1$, and $n_{\mathrm{S}} = 1.44$.

The dispersion relation of the $\mathrm{TM}_0$ guided mode is shown by the black solid line in Fig. 2(b). The cutoff angular frequency of the $\mathrm{TM}_0$ guided mode is $\omega_{\mathrm{c,\,TM}_0} = 0.1658\omega_0$. The dispersion relations $k_{x,+1}$ and $k_{x,+2}$ are shown by the blue and red dashed lines in Fig. 2(b). As demonstrated, there are two crossing points, which are marked by $B_{+1}$ and $B_{+2}$. The corresponding angular frequencies are $\omega_{+1} = 0.2150\omega_0$ ($\lambda_{+1} = 1483.7$ nm) and $\omega_{+2} = 0.3884\omega_0$ ($\lambda_{+2} = 823.9$ nm). At these two angular frequencies, the GMR condition is satisfied and gives rise to Fano resonances.

When the tunable geometric parameter $\Delta = 0$, the widths of two air grooves are the same ($w_{\mathrm{L1}} = w_{\mathrm{L2}}$). Hence, the four-part period grating layer reduces to a two-part period grating layer. The period of the grating becomes $\Lambda' = \Lambda/2$. As a result, the grating-induced tangential wave vector becomes $m' \times (2\pi/\Lambda') = m' \times (4\pi/\Lambda)$. The GMR condition turns into

$$k_{x,m'} = k_0 \sin\theta - m'\frac{4\pi}{\Lambda} = \beta \;(m' = \pm 1,\ \pm 2, \ldots). \quad (4)$$

In the case of $s$ polarization, the dispersion relation $k'_{x,+1}$ is shown by the blue dotted line in Fig. 2(c). Clearly, the dispersion relation $k'_{x,+1}$ overlaps with the previous dispersion relation $k_{x,+2}$ since the grating-induced tangential wave vector doubles. Now, there is only one crossing point, which is marked by $A'_{+1}$ (previous $A_{+2}$). As the tunable geometric parameter changes $\Delta$ from a nonzero value to zero, the previous excitable guided resonance at point $A_{+1}$ ($\lambda_{+1} = 1578.7$ nm) becomes unexcitable. Based on such selectable guided resonance, a BIC can be theoretically realized. However, the previous excitable guided resonance at point $A_{+2}$ ($\lambda_{+2} = 859.3$ nm) is still excitable, giving rise to a conventional Fano resonance.

In the case of $p$ polarization, the situation is similar. In Fig. 2(d), the blue dotted line represents the dispersion relation $k'_{x,+1}$. Now, there is only one crossing point, which is marked by $B'_{+1}$ (previous $B_{+2}$). As the tunable geometric parameter $\Delta$ changes from a nonzero value to zero, the previous excitable guided resonance at point $B_{+1}$ ($\lambda_{+1} = 1483.7$ nm) becomes unexcitable. Based on such selectable guided resonance, a BIC can be theoretically realized. However, the previous excitable guided resonance at point $B_{+2}$ ($\lambda_{+2} = 823.9$ nm) is still excitable, giving rise to a conventional Fano resonance. Owing to the polarization-dependent property of the dispersion relation of the guided mode, the BIC is also polarization dependent.

Then, based on the rigorous coupled-wave analysis [86,87], we calculate the reflectance spectra of the compound

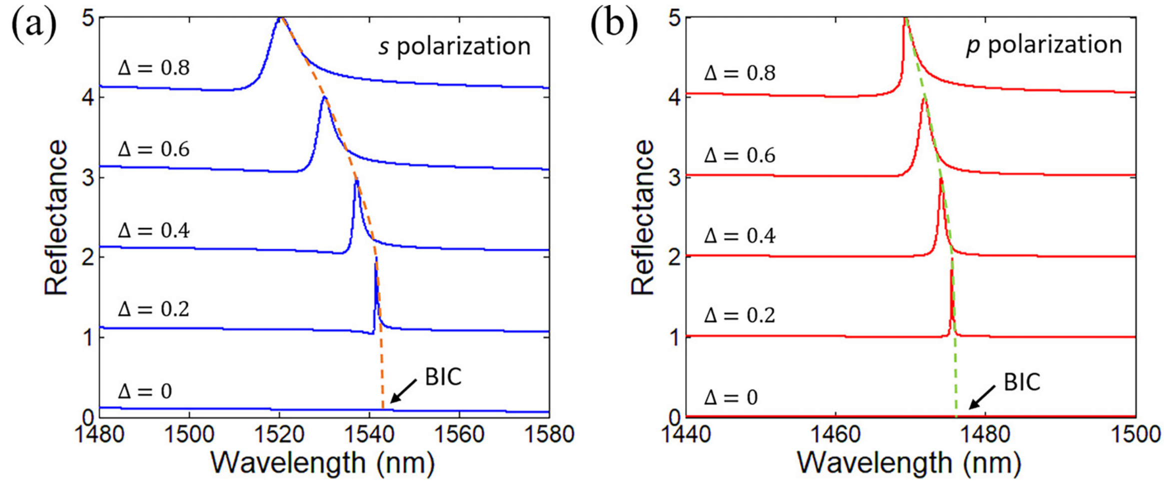


FIG. 3. Reflectance spectra of the compound grating waveguide structure under (a) $s$ and (b) $p$ polarizations for different $\Delta$. Other parameters are set to be $\Lambda = 962$ nm, $w_H = f_H\Lambda = 0.3\Lambda$, $h_G = 750$ nm, $h_{WG} = 320$ nm, $n_H = 1.88$, $n_L = 1$, and $n_S = 1.44$.

grating waveguide structure under $s$ and $p$ polarizations for different $\Delta$ as shown in Figs. 3(a) and 3(b), respectively. For better visuality, the reflectance curves are shifted in the unit of 1. Under $s$ polarization, a Fano peak occurs at the wavelength $\lambda = 1520.5$ nm when $\Delta = 0.8$. As $\Delta$ decreases, the resonance width of the Fano peak reduces rapidly. As $\Delta$ continues to decrease to zero, the resonance width vanishes completely, which indicates that a BIC appears. The BIC wavelength under $s$ polarization can be extracted as $\lambda = 1543.2$ nm, which slightly deviates from the BIC wavelength predicted by the GMR condition ($\lambda_{+1} = 1578.7$ nm). The relative error is only 2.25%. The underlying reason is that the top grating layer slightly changes the effective refractive index of the waveguide layer [84]. Under $p$ polarization, a Fano peak occurs at the wavelength $\lambda = 1469.4$ nm when $\Delta = 0.8$. As $\Delta$ decreases, the resonance width of the Fano peak reduces rapidly. As $\Delta$ continues to decrease to zero, the resonance width vanishes completely, which indicates that a BIC appears. The BIC wavelength under $p$ polarization ($\lambda = 1476.1$ nm) slightly deviates from the BIC wavelength predicted by the GMR condition ($\lambda_{+1} = 1483.7$nm). The relative error is only 0.51%. It is known that the electric-field distributions in compound grating waveguide structure under $s$ and $p$ polarizations are different. Hence, the degrees of the change of the effective refractive index of the waveguide layer under $s$ and $p$ polarizations when a top grating layer is introduced are also different. As a result, the relative errors of the BIC wavelength under $s$ and $p$ polarizations are different.

Next, we calculate the dependences of the $Q$ factor of the quasi-BIC on $\Delta$ under $s$ and $p$ polarizations as, respectively, shown in Figs. 4(a) and 4(b). The $Q$ factor is calculated by [88]

$$Q = \frac{f_{\text{peak}}}{\Delta f} = \frac{f_{\text{peak}}}{|f_{\text{peak}} - f_{\text{dip}}|}, \tag{5}$$

where $f_{\text{peak}}$ represents the frequency of the reflectance peak, $f_{\text{dip}}$ represents the frequency of the reflectance dip, and $\Delta f = |f_{\text{peak}} - f_{\text{dip}}|$ represents the resonance width. Under $s$ polarization, the $Q$ factor is $9.7 \times 10^2$ when $\Delta = 0.25$. As $\Delta$ gradually decreases to near zero, the $Q$ factor increases dramatically. When $\Delta = 0.02$, the $Q$ factor reaches $1.5 \times 10^5$. When $\Delta = 0$, the $Q$ factor becomes infinite. Under $p$ polarization, the $Q$ factor is $3.9 \times 10^2$ when $\Delta = 0.25$. As $\Delta$ gradually decreases to near zero, the $Q$ factor also increases dramatically. When $\Delta = 0.02$, the $Q$ factor reaches $3.7 \times 10^4$. When $\Delta = 0$, the $Q$ factor becomes infinite. According to the perturbation theory, the $Q$ factor of the quasi-BIC is proportional to the negative quadratic power of the perturbation parameter, i.e., $Q \propto \Delta^{-2}$ [61]. Hence, the $Q$ factor of the quasi-BIC dramatically increases as the perturbation parameter $\Delta$ approaches to zero.

## III. GIANT PSHE EMPOWERED BY POLARIZATION-DEPENDENT QUASI-BICS

In this section, we utilize the polarization-dependent quasi-BIC to enhance the PSHE. Figure 5 schematically illustrates the PSHE when a linearly polarized Gaussian beam obliquely launches onto the compound grating waveguide structure with the incident angle $\theta = 5^\circ$. The $z$ axis of the laboratory Cartesian frame $(x, y, z)$ is perpendicular to the interface of the waveguide layer. The incident and reflected electric fields are presented in Cartesian frames $(x_i, y_i, z_i)$ and $(x_r, y_r, z_r)$, respectively. $\delta_\mp$ represent the transverse shifts of the left and right circularly polarized components, respectively. In the spin basis set, the angular spectrum of the incident Gaussian beam can be expressed as

$$\tilde{\boldsymbol{E}}_i^H = \frac{1}{\sqrt{2}}(\tilde{\boldsymbol{E}}_{i+} + \tilde{\boldsymbol{E}}_{i-}), \tag{6a}$$

$$\tilde{\boldsymbol{E}}_i^V = \frac{j}{\sqrt{2}}(\tilde{\boldsymbol{E}}_{i+} - \tilde{\boldsymbol{E}}_{i-}). \tag{6b}$$

Here, the superscripts $H$ and $V$ represent horizontal and vertical polarizations, respectively. The subscripts $\pm$ represent the left and right circularly polarized components, respectively. $j$ represents the imaginary unit. Supposing that the beam waist of the incident Gaussian beam is $w_0$, we have

$$\tilde{\boldsymbol{E}}_{i\pm} = \frac{w_0}{\sqrt{2\pi}}\exp\left[-\frac{w_0^2\left(k_{ix}^2 + k_{iy}^2\right)}{4}\right](\boldsymbol{e}_{ix} \pm j\boldsymbol{e}_{iy}). \tag{7}$$

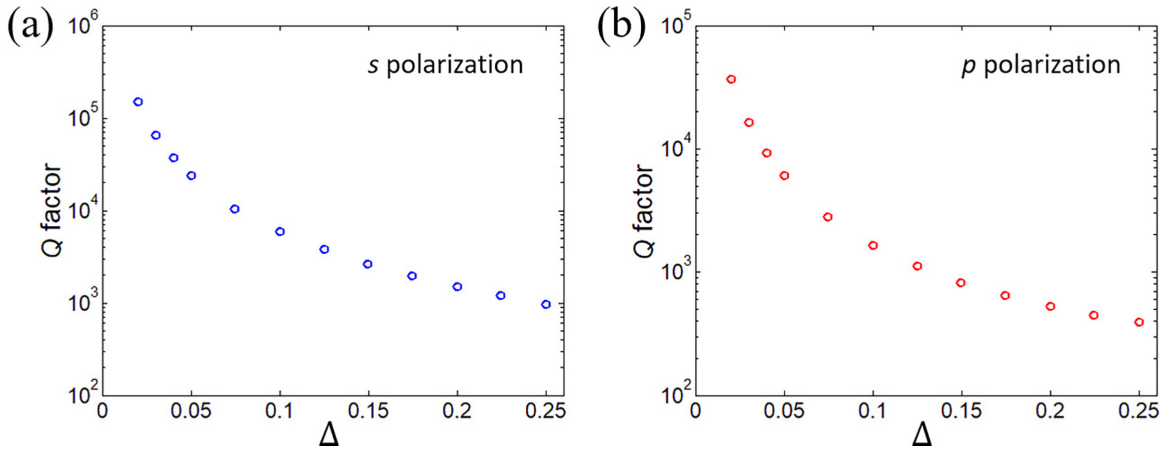


FIG. 4. Dependences of the $Q$ factor of the quasi-BIC on $\Delta$ under (a) $s$ and (b) $p$ polarizations. Other parameters are set to be $\Lambda = 962$ nm, $w_{\mathrm{H}} = f_{\mathrm{H}}\Lambda = 0.3\Lambda$, $h_{\mathrm{G}} = 750$ nm, $h_{\mathrm{WG}} = 320$ nm, $n_{\mathrm{H}} = 1.88$, $n_{\mathrm{L}} = 1$, and $n_{\mathrm{S}} = 1.44$.

According to Appendix A in Ref. [89], the angular spectrum of the reflected beam and that of the incident beam can be related by a $2 \times 2$ matrix:

$$\begin{bmatrix} \tilde{E}_r^H \\ \tilde{E}_r^V \end{bmatrix} = \begin{bmatrix} r_p & \frac{k_{ry}}{k_0}(r_p + r_s)\cot\theta \\ -\frac{k_{ry}}{k_0}(r_p + r_s)\cot\theta & r_s \end{bmatrix} \begin{bmatrix} \tilde{E}_i^H \\ \tilde{E}_i^V \end{bmatrix}, \tag{8}$$

where $r_s$ and $r_p$ represent, respectively, the reflection coefficients of the compound grating waveguide structure under $s$ and $p$ polarizations. It should be noted that the incident plane is $xOz$ plane in our work. There is no polarization conversion effect between linearly polarized lights [86]. Therefore, Eq. (8) is still applicable for compound grating waveguide structures [90].

Supposing that the incident Gaussian beam is wide enough (the angular spectrum is narrow enough), we can obtain the expressions of the angular spectrum of the reflected beam [89]:

$$\tilde{\boldsymbol{E}}_r^H = \frac{r_p}{\sqrt{2}}\left[\exp\left(+jk_{ry}\delta_r^H\right)\tilde{\boldsymbol{E}}_{r+} + \exp\left(-jk_{ry}\delta_r^H\right)\tilde{\boldsymbol{E}}_{r-}\right], \tag{9a}$$

$$\tilde{\boldsymbol{E}}_r^V = \frac{jr_s}{\sqrt{2}}\left[-\exp\left(+jk_{ry}\delta_r^V\right)\tilde{\boldsymbol{E}}_{r+} + \exp\left(-jk_{ry}\delta_r^V\right)\tilde{\boldsymbol{E}}_{r-}\right], \tag{9b}$$

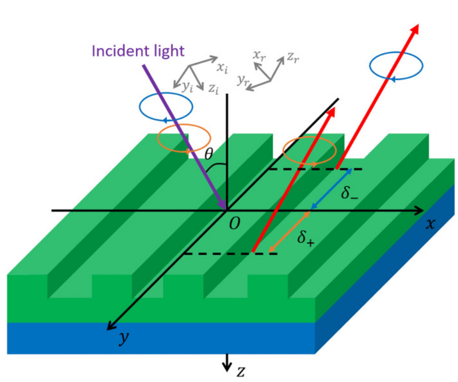


FIG. 5. Schematic of the PSHE when a linearly polarized Gaussian beam launches onto the compound grating waveguide structure. $\delta_{\mp}$ represent, respectively, the transverse shifts of the left and right circularly polarized components.

where

$$\delta_r^H = \frac{\lambda}{2\pi}\left(1 + \frac{r_s}{r_p}\right)\cot\theta, \tag{10a}$$

$$\delta_r^V = \frac{\lambda}{2\pi}\left(1 + \frac{r_p}{r_s}\right)\cot\theta, \tag{10b}$$

$$\tilde{\boldsymbol{E}}_{r\pm} = \frac{w_0}{\sqrt{2\pi}}\exp\left[-\frac{w_0^2\left(k_{rx}^2 + k_{ry}^2\right)}{4}\right](\boldsymbol{e}_{rx} \pm j\boldsymbol{e}_{ry}). \tag{11}$$

Here, $\lambda$ represents the wavelength of the incident Gaussian beam.

As seen from Eqs. (9a) and (9b), the terms $\exp(\pm jk_{ry}\delta_r^H)$ and $\exp(\pm jk_{ry}\delta_r^V)$ represent the spin-orbit interaction terms under horizontal and vertical polarizations, respectively. Clearly, the real parts of the spin-orbit interaction terms represent the transverse shifts of the PSHE under horizontal and vertical polarizations. Hence, we have

$$\delta_{\pm}^H = \mp\mathrm{Re}\left(\delta_r^H\right) = \mp\frac{\lambda}{2\pi}\left[1 + \frac{|r_s|}{|r_p|}\cos(\varphi_s - \varphi_p)\right]\cot\theta, \tag{12a}$$

$$\delta_{\pm}^V = \mp\mathrm{Re}\left(\delta_r^V\right) = \mp\frac{\lambda}{2\pi}\left[1 + \frac{|r_p|}{|r_s|}\cos(\varphi_p - \varphi_s)\right]\cot\theta, \tag{12b}$$

where $r_s = |r_s|\exp(j\varphi_s)$ and $r_p = |r_p|\exp(j\varphi_p)$. Notice that Eqs. (12a) and (12b) are only applicable when the incident Gaussian beam is wide enough. Under current experimental condition, it is not difficult to generate a Gaussian beam with the width of 750 μm [91].

Now, we consider the intrinsic and scattering losses of $HfO_2$. According to the experimental measurement on the optical constant of the $HfO_2$ thin film [92,93], the extinction coefficient of $HfO_2$ at near-infrared wavelengths is lower than or equal to the order of $10^{-6}$. Such nonzero extinction coefficient is mainly contributed by the intrinsic loss of $HfO_2$. However, for the grating structure, both the intrinsic and scattering losses should be considered. According to the measured reflectance spectrum of the $HfO_2$-based grating structure [94], the total extinction coefficient of $HfO_2$ contributed by the intrinsic and scattering losses can be

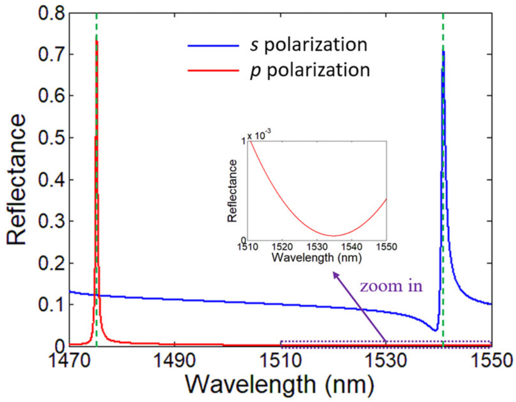


FIG. 6. Reflectance spectra of the compound grating waveguide structure under $s$ and $p$ polarizations for $\Delta = 0.25$. Other parameters are set to be $\Lambda = 962$ nm, $w_{\mathrm{H}} = f_{\mathrm{H}}\Lambda = 0.3\Lambda$, $h_{\mathrm{G}} = 750$ nm, $h_{\mathrm{WG}} = 320$ nm, $n_{\mathrm{H}} = 1.88 + 10^{-4}j$, $n_{\mathrm{L}} = 1$, and $n_{\mathrm{S}} = 1.44$. Two green dashed lines represent the positions of the quasi-BICs under $s$ and $p$ polarizations.

fitted as $\kappa_{\mathrm{H}} = 3 \times 10^{-5}$. In this work, the extinction coefficient of $HfO_2$ is selected as a higher value, $\kappa_{\mathrm{H}} = 10^{-4}$. Hence, the refractive index of $HfO_2$ becomes $n_{\mathrm{H}} = 1.88 + j\kappa_{\mathrm{H}} = 1.88 + 10^{-4}j$. As we discussed in Sec. II, to obtain a polarization-dependent quasi-BIC, the geometric parameter $\Delta$ should be set to be nonzero. Since the geometric parameter $\Delta = (w_{\mathrm{L1}} - w_{\mathrm{L2}})/(w_{\mathrm{L1}} + w_{\mathrm{L2}})$ reflects the width difference between two air grooves, a smaller geometric parameter $\Delta$ makes the fabrication more difficult. Considering the difficulty of the fabrication, we set the geometric parameter to be $\Delta = 0.25$. The widths of two air grooves are $w_{\mathrm{L1}} = f_{\mathrm{L1}}\Lambda = 0.25\Lambda$ and $w_{\mathrm{L2}} = f_{\mathrm{L2}}\Lambda = 0.15\Lambda$, respectively. The width difference between two air grooves reaches $\Delta w = w_{\mathrm{L1}} - w_{\mathrm{L2}} = 0.1\Lambda = 96.2$ nm, which is well within the reach of current fabrication technique [95]. Figure 6 gives the reflectance spectra of the compound grating waveguide structure under $s$ and $p$ polarizations. As marked by two green dashed lines, the quasi-BIC under $s$ polarization is located at the wavelength $\lambda = 1540.9$ nm while that under $p$ polarization is located at the wavelength $\lambda = 1475.3$ nm. Owing to the optical loss of $HfO_2$, the reflectance does not reach unity. The wavelength difference of the quasi-BICs under $s$ and $p$ polarizations reaches $\Delta\lambda = 65.6$ nm. The $Q$ factors of the quasi-BICs under $s$ and $p$ polarizations are $1.0 \times 10^3$ and $4.0 \times 10^2$, respectively. Under current fabrication technique, the measured $Q$ factors of the quasi-BICs can reach or exceed the order of $10^4$ [65,95].

According to Eq. (12a), the terms $|r_s|/|r_p|$ and $\cos(\varphi_s - \varphi_p)$ play dominant roles in the transverse shift

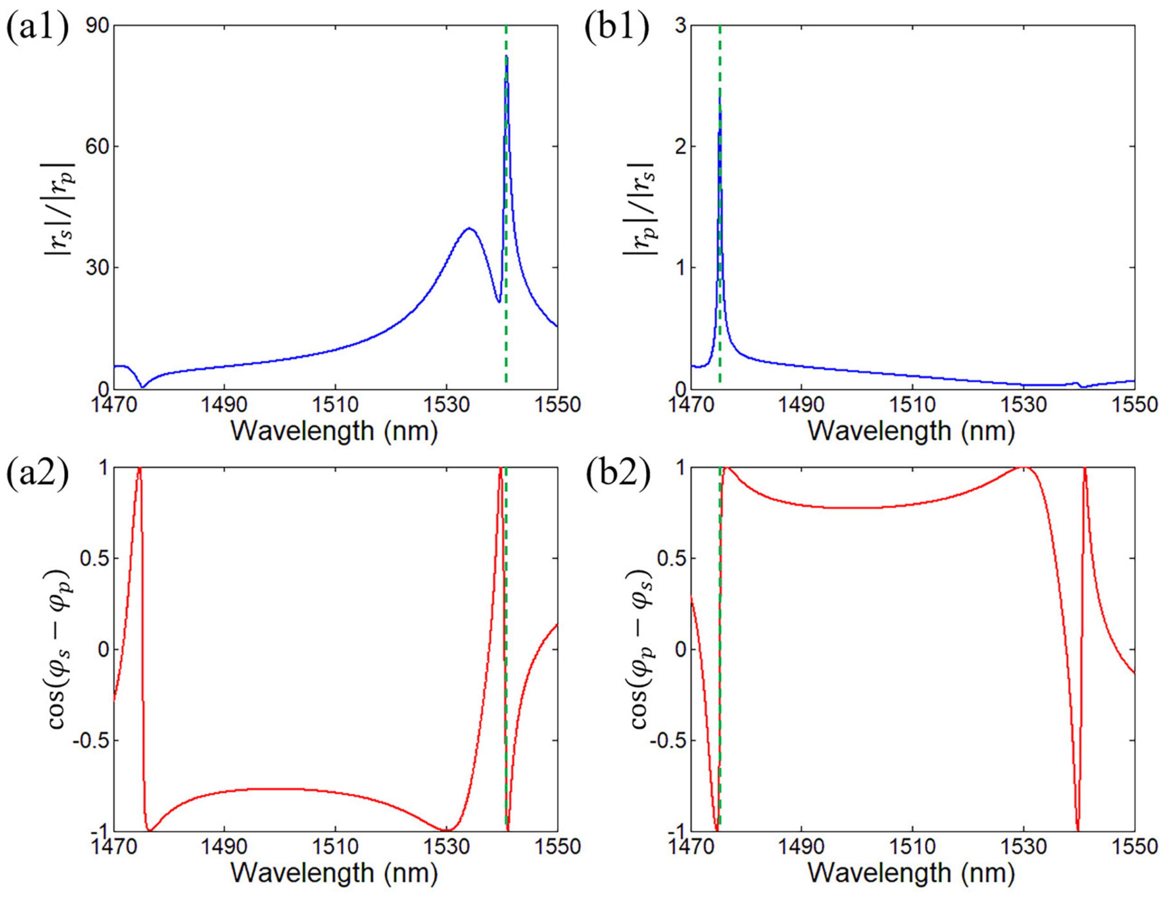


FIG. 7. (a1) $|r_s|/|r_p|$, (a2) $\cos(\varphi_s - \varphi_p)$, (b1) $|r_p|/|r_s|$, and (b2) $\cos(\varphi_p - \varphi_s)$ as functions of the wavelength for $\Delta = 0.25$. Other parameters are set to be $\Lambda = 962$ nm, $w_{\mathrm{H}} = f_{\mathrm{H}}\Lambda = 0.3\Lambda$, $h_{\mathrm{G}} = 750$ nm, $h_{\mathrm{WG}} = 320$ nm, $n_{\mathrm{H}} = 1.88 + 10^{-4}j$, $n_{\mathrm{L}} = 1$, and $n_{\mathrm{S}} = 1.44$. Green dashed lines in (a1) and (a2) represent the position of the quasi-BIC under $s$ polarization. Green dashed lines in (b1) and (b2) represent the position of the quasi-BIC under $p$ polarization.

of the PSHE under horizontal polarization $\delta_+^H$. In Figs. 7(a1) and 7(a2), we give $|r_s|/|r_p|$ and $\cos(\varphi_s-\varphi_p)$ as functions of the wavelength, respectively. The green dashed line represents the position of the quasi-BIC for $s$ polarization, i.e., $\lambda = 1540.9$ nm. At the quasi-BIC wavelength under $s$ polarization, $|r_s|/|r_p|$ reaches its maximum 82.38 since $|r_s| = \sqrt{R_s}$ reaches 0.85 and $|r_p| = \sqrt{R_p}$ is only 0.010. Notice that a secondary peak of $|r_s|/|r_p|$ occurs at the wavelength $\lambda = 1534.2$ nm. The reason of the formation of the secondary peak can be explained as follows. As shown in the inset of Fig. 6, a dip of $|r_p|$ occurs at the wavelength $\lambda = 1534.8$ nm. The minimum of $|r_p|$ is only 0.0067. At the wavelength $\lambda = 1534.2$ nm, $|r_s|$ reaches 0.27 and $|r_p|$ is only 0.0068. Hence, $|r_s|/|r_p|$ still reaches 39.59. Around the quasi-BIC wavelengths under $s$ and $p$ polarizations, $\cos(\varphi_s-\varphi_p)$ changes dramatically due to the resonances of the quasi-BICs. Similarly, according to Eq. (12b), the terms $|r_p|/|r_s|$ and $\cos(\varphi_p-\varphi_s)$ play dominant roles in the transverse shift of the PSHE under vertical polarization $\delta_+^V$. In Figs. 7(b1) and 7(b2), we give $|r_p|/|r_s|$ and $\cos(\varphi_p-\varphi_s)$ as functions of the wavelength, respectively. The green dashed line represents the position of the quasi-BIC for $p$ polarization, i.e., $\lambda = 1475.3$ nm. At the quasi-BIC wavelength under $p$ polarization, $|r_p|/|r_s|$ reaches its maximum 2.47 since $|r_p|$ reaches 0.86 and $|r_s|$ is 0.35. Notice that $|r_s|$ at the quasi-BIC wavelength under $p$ polarization is much higher than $|r_p|$ at the quasi-BIC wavelength under $s$ polarization. Therefore, the maximum of $|r_p|/|r_s|$ is much lower than the maximum of $|r_s|/|r_p|$. Around the quasi-BIC wavelengths under $s$ and $p$ polarizations, $\cos(\varphi_p-\varphi_s)$ changes dramatically due to the resonances of the quasi-BICs.

Then, we calculate the transverse shifts of the PSHE $\delta_+^H$ and $\delta_+^V$ as functions of the wavelength according to Eqs. (12a) and (12b), as shown in Figs. 8(a) and 8(b). The green dashed line in Fig. 8(a) represents the position of the quasi-BIC for $s$ polarization, i.e., $\lambda = 1540.9$ nm. The green dashed line in Fig. 8(b) represents the position of the quasi-BIC for $p$ polarization, i.e., $\lambda = 1475.3$ nm. Both the values of the terms $|r_s|/|r_p|$ and $\cos(\varphi_s-\varphi_p)$ determine the value of $\delta_+^H$. Since $-1 \leqslant \cos(\varphi_s-\varphi_p) \leqslant 1$, the sign of $\delta_+^H$ can be positive or negative. At the wavelength $\lambda = 1541.0$ nm, $\delta_+^H$ reaches its positive maximum 215.3 μm since $|r_s|/|r_p|$ is close to its maximum and $\cos(\varphi_s-\varphi_p)$ is close to $-1$. Owing to the resonance of the quasi-BIC under $s$ polarization, $\delta_+^H$ changes dramatically at the wavelength $\lambda = 1541.0$ nm. Hence, if one would like to observe a giant $\delta_+^H$ in experiments, the wavelength resolution of the spectrophotometer is required to be relatively high. At the wavelength $\lambda = 1532.4$ nm, $\delta_+^H$ reaches 95.9 μm since $|r_s|/|r_p|$ is close to the value of the secondary peak of $|r_s|/|r_p|$ and $\cos(\varphi_s-\varphi_p)$ is close to $-1$. The resonance width of the secondary peak of $\delta_+^H$ is wider than that of the main peak of $\delta_+^H$, which could be easier to be observed in experiments. At the wavelength $\lambda = 1540.2$ nm, $\delta_+^H$ reaches its negative maximum, $-86.1$ μm. Similarly, both the values of the terms $|r_p|/|r_s|$ and $\cos(\varphi_p-\varphi_s)$ determine the value of $\delta_+^V$. Since $-1 \leqslant \cos(\varphi_p-\varphi_s) \leqslant 1$, the sign of $\delta_+^V$ can be positive or negative. At the wavelength $\lambda = 1475.1$ nm, $\delta_+^V$ reaches its negative maximum, $-6.6$ μm, since $|r_p|/|r_s|$ is close to its maximum and $\cos(\varphi_p-\varphi_s)$ is close to 1. At the

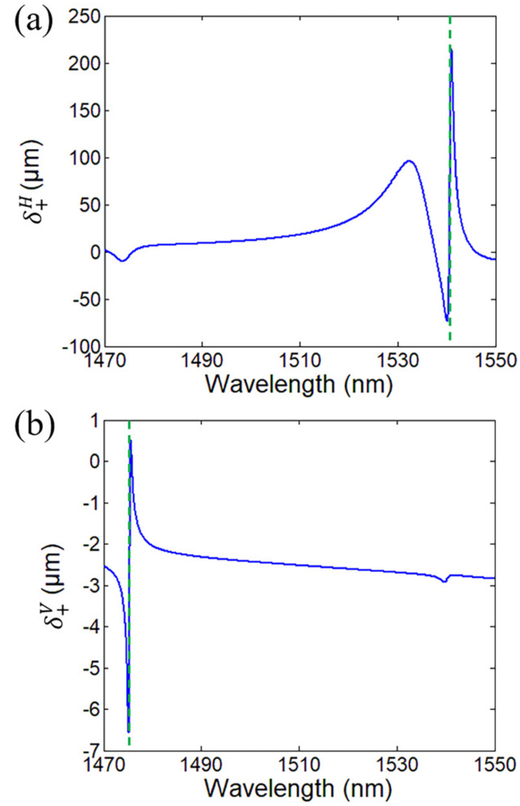


FIG. 8. Transverse shifts of the PSHE (a) $\delta_+^H$ and (b) $\delta_+^V$ as functions of the wavelength for $\Delta = 0.25$. Other parameters are set to be $\Lambda = 962$ nm, $w_\mathrm{H} = f_\mathrm{H}\Lambda = 0.3\Lambda$, $h_\mathrm{G} = 750$ nm, $h_\mathrm{WG} = 320$ nm, $n_\mathrm{H} = 1.88 + 10^{-4}j$, $n_\mathrm{L} = 1$, and $n_\mathrm{S} = 1.44$. Green dashed lines in (a) and (b) represent the positions of the quasi-BICs under $s$ and $p$ polarizations, respectively.

wavelength $\lambda = 1475.6$ nm, $\delta_+^V$ reaches its positive maximum, 0.5 μm. Notice that the enhancement of the transverse shift of the PSHE under vertical polarization $\delta_+^V$ is much weaker than that under horizontal polarization $\delta_+^H$. If we select other geometric parameters of the compound grating waveguide structure, the enhancement of the transverse shift of the PSHE under vertical polarization $\delta_+^V$ can be much stronger than that under horizontal polarization $\delta_+^H$.

Finally, we discuss the influences of the geometric parameters $\Lambda$, $h_\mathrm{G,}$ and $h_\mathrm{WG}$ on the positive maximum of $\delta_+^H$. Figure 9(a) gives the dependence of the geometric parameter $\Lambda$ on $\max(\delta_+^H)$. Two other geometric parameters, $h_\mathrm{G} = 750$ nm and $h_\mathrm{WG} = 320$ nm, are kept unchanged. As the period of the grating layer $\Lambda$ changes within $960 \pm 10$ nm, $\max(\delta_+^H)$ ranges from 109.6 to 280.5 μm. Figure 9(b) gives the dependence of the geometric parameter $h_\mathrm{G}$ on $\max(\delta_+^H)$. Two other geometric parameters, $\Lambda = 962$ nm and $h_\mathrm{WG} = 320$ nm, are kept unchanged. As the height of the grating layer $h_\mathrm{G}$ changes within $740 \pm 10$ nm, $\max(\delta_+^H)$ ranges from 54.9 to 215.3 μm. Figure 9(c) gives the dependence of the geometric parameter $h_\mathrm{WG}$ on $\max(\delta_+^H)$. Two other geometric parameters, $\Lambda = 962$ nm and $h_\mathrm{G} = 750$ nm, are kept unchanged. As the height of the waveguide layer $h_\mathrm{WG}$ changes within $320 \pm 10$ nm, $\max(\delta_+^H)$ ranges from 72.3 to 217.3 μm. Therefore, when considering the geometric parameter errors during the fabrication

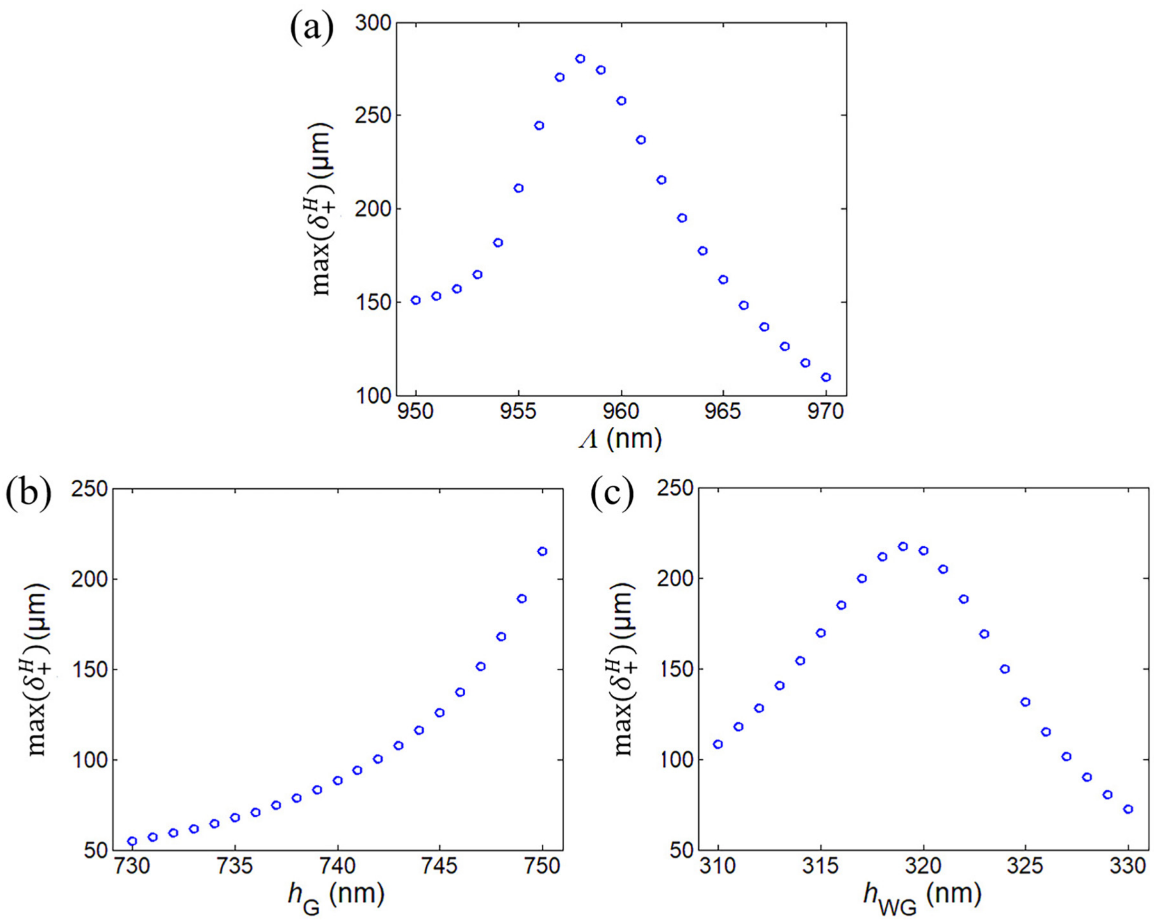


FIG. 9. Dependences of the geometric parameters (a) $\Lambda$, (b) $h_\mathrm{G}$, and (c) $h_\mathrm{WG}$ on $\max(\delta_+^H)$ for $\Delta = 0.25$.

process, the transverse shift of the PSHE can be at least on the order of dozens of micrometers.

## IV. CONCLUSIONS

In summary, we theoretically propose a BIC in a compound grating waveguide structure based on the selectable guided resonance at near-infrared wavelengths. Owing to the polarization-dependent property of the dispersion relation of the guided mode, the BIC is also polarization dependent. Empowered by the polarization-dependent quasi-BIC, the transverse shift of the PSHE can be greatly enhanced to the order of hundreds of micrometers. In addition, the enhancement of the transverse shift of the PSHE is robust against the period of the grating layer, the height of the grating layer, and the height of the waveguide layer. These results provide a feasible route to achieving giant PSHE and designing high-performance PSHE-based optical devices.

## ACKNOWLEDGMENTS

This work is sponsored by the National Natural Science Foundation of China (Grants No. 12104105, No. 12264028, No. 11947065, and No. 61901164), the Science and Technology Program of Guangzhou (Grant No. 202201011176), the Guangdong Basic and Applied Basic Research Foundation (Grant No. 2023A1515011024), the Special Projects in Key Fields of Universities in Guangdong Province (Grant No. 2020ZDZX3048), the Natural Science Foundation of Jiangxi Province (Grant No. 20202BAB211007), the China Scholarship Council (Grant No. 202008420045), the Start-up Funding of Guangdong Polytechnic Normal University (Grant No. 2021SDKYA033), and the Interdisciplinary Innovation Fund of Nanchang University (Grant No. 2019-9166-27060003). F.W. would like to thank a mathematician engaged in the Landau-Siegel zero conjecture, Yitang Zhang, for his tenacious spirit of exploration.

[1] M. Onoda, S. Murakami, and N. Nagaosa, Hall Effect of Light, Phys. Rev. Lett. **93**, 083901 (2004).

[2] K. Yu. Bliokh and Y. P. Bliokh, Conservation of Angular Momentum, Transverse Shift, and Spin Hall Effect in Reflection and Refraction of an Electromagnetic Wave Packet, Phys. Rev. Lett. **96**, 073903 (2006).

[3] H. Luo, S. Wen, W. Shu, Z. Tang, Y. Zou, and D. Fan, Spin Hall effect of a light beam in left-handed materials, Phys. Rev. A **80**, 043810 (2009).

[4] X. Ling, X. Zhou, K. Huang, Y. Liu, C.-W. Qiu, H. Luo, and S. Wen, Recent advances in the spin Hall effect of light, Rep. Prog. Phys. **80**, 066401 (2017).

[5] D. Haefner, S. Sukhov, and A. Dogariu, Spin Hall Effect of Light in Spherical Geometry, Phys. Rev. Lett. **102**, 123903 (2009).

[6] Y. Qin, Y. Li, X. Feng, Z. Liu, H. He, Y.-F. Xiao, and Q. Gong, Spin Hall effect of reflected light at the air-uniaxial crystal interface, Opt. Express **18**, 16832 (2010).

[7] J. Korger, A. Aiello, V. Chille, P. Banzer, C. Wittmann, N. Lindlein, C. Marquardt, and G. Leuchs, Observation of the Geometric Spin Hall Effect of Light, Phys. Rev. Lett. **112**, 113902 (2014).

[8] W. Luo, S. Xiao, Q. He, S. Sun, and L. Zhou, Photonic spin Hall effect with nearly 100% efficiency, Adv. Opt. Mater. **3**, 1102 (2015).

[9] K. Y. Bliokh, F. J. Rodríguez-Fortuño, F. Nori, and A. V. Zayats, Spin-orbit interactions of light, Nat. Photonics **9**, 796 (2015).

[10] A. V. Nalitov, G. Malpuech, H. Terças, and D. D. Solnyshkov, Spin-orbit Coupling and the Optical Spin Hall Effect in Photonic Graphene, Phys. Rev. Lett. **114**, 026803 (2015).

[11] Y.-H. Wang, R.-C. Jin, J.-Q. Li, F. Zhong, H. Liu, I. Kim, Y. Jo, J. Rho, and Z.-G. Dong, Photonic spin Hall effect by the spin-orbit interaction in a metasurface with elliptical nano-structures, Appl. Phys. Lett. **110**, 101908 (2017).

[12] X. Zhou, L. Sheng, and X. Ling, Photonic spin Hall effect enabled refractive index sensor using weak measurements, Sci. Rep. **8**, 1221 (2018).

[13] R. Wang, J. Zhou, K. Zeng, S. Chen, X. Ling, W. Shu, H. Luo, and S. Wen, Ultrasensitive and real-time detection of chemical reaction rate based on the photonic spin Hall effect, APL Photonics **5**, 016105 (2020).

[14] W. Zhu, H. Xu, J. Pan, S. Zhang, H. Zheng, Y. Zhong, J. Yu, and Z. Chen, Black phosphorus terahertz sensing based on photonic spin Hall effect, Opt. Express **28**, 25869 (2020).

[15] A. Srivastava, A. K. Sharma, and Y. K. Prajapati, On the sensitivity-enhancement in plasmonic biosensor with photonic spin Hall effect at visible wavelength, Chem. Phys. Lett. **774**, 138613 (2021).

[16] X. Zhou, Z. Xiao, H. Luo, and S. Wen, Experimental observation of the spin Hall effect of light on a nanometal film via weak measurements, Phys. Rev. A **85**, 043809 (2012).

[17] S. Chen, X. Ling, W. Shu, H. Luo, and S. Wen, Precision Measurement of the Optical Conductivity of Atomically Thin Crystals Via the Photonic Spin Hall Effect, Phys. Rev. Appl. **13**, 014057 (2020).

[18] J.-M. Ménard, A. E. Mattacchione, H. M. van Driel, C. Hautmann, and M. Betz, Ultrafast optical imaging of the spin Hall effect of light in semiconductors, Phys. Rev. B **82**, 045303 (2010).

[19] S. He, J. Zhou, S. Chen, W. Shu, H. Luo, and S. Wen, Spatial differential operation and edge detection based on the geometric spin Hall effect of light, Opt. Lett. **45**, 877 (2020).

[20] C.-F. Li, Unified theory for Goos-Hänchen and Imbert-Fedorov effects, Phys. Rev. A **76**, 013811 (2007).

[21] A. Aiello and J. P. Woerdman, Role of beam propagation in Goos-Hänchen and Imbert-Fedorov shifts, Opt. Lett. **33**, 1437 (2008).

[22] K. Y. Bliokh and A. Aiello, Goos-Hänchen and Imbert-Fedorov beam shifts: An overview, J. Opt. **15**, 014001 (2013).

[23] G. Jayaswal, G. Mistura, and M. Merano, Observation of the Imbert-Fedorov effect via weak value amplification, Opt. Lett. **39**, 2266 (2014).

[24] Q.-D. Jiang, H. Jiang, H. Liu, Q.-F. Sun, and X. C. Xie, Topological Imbert-Fedorov Shift in Weyl Semimetals, Phys. Rev. Lett. **115**, 156602 (2015).

[25] W. Zhen and D. Deng, Goos-Hänchen and Imbert-Fedorov shifts in temporally dispersive attenuative materials, J. Phys. D: Appl. Phys. **53**, 255104 (2020).

[26] F. I. Fedorov, K Teorii Polnogo Otrazheniya, Dokl. Akad. Nauk SSSR **105**, 465 (1955) [To the theory of total reflection, J. Opt. **15**, 014002 (2013)].

[27] C. Imbert, Calculation and experimental proof of the transverse shift induced by total internal reflection of a circularly polarized light beam, Phys. Rev. D **5**, 787 (1972).

[28] F. Pillon, H. Gilles, and S. Girard, Experimental observation of the Imbert-Fedorov transverse displacement after a single total reflection, Appl. Opt. **43**, 1863 (2004).

[29] N. Hermosa, A. M. Nugrowati, A. Aiello, and J. P. Woerdman, Spin Hall effect of light in metallic reflection, Opt. Lett. **36**, 3200 (2011).

[30] O. Hosten and P. Kwiat, Observation of the spin Hall effect of light via weak measurements, Science **319**, 787 (2008).

[31] O. Takayama and G. Puentes, Enhanced spin Hall effect of light by transmission in a polymer, Opt. Lett. **43**, 1343 (2018).

[32] M. Neugebauer, S. Nechayev, M. Vorndran, G. Leuchs, and P. Banzer, Weak measurement enhanced spin Hall effect of light for particle displacement sensing, Nano Lett. **19**, 422 (2019).

[33] J. Li, T. Tang, L. Luo, J. Shen, C. Li, J. Qin, and L. Bi, Weak measurement of the magneto-optical spin Hall effect of light, Photonics Res. **7**, 1014 (2019).

[34] M. Kim, D. Lee, Y. Kim, and J. Rho, Nanophotonic-assisted precision enhancement of weak measurement using spin Hall effect of light, Nanophotonics **11**, 4591 (2022).

[35] X. Yin, Z. Ye, J. Rho, Y. Wang, and X. Zhang, Photonic spin Hall effect at metasurfaces, Science **339**, 1405 (2013).

[36] A. Shaltout, J. Liu, A. Kildishev, and V. Shalaev, Photonic spin Hall effect in gap-plasmon metasurfaces for on-chip chiroptical spectroscopy, Optica **2**, 860 (2015).

[37] K. Chaudhuri, A. Shaltout, D. Shah, U. Guler, A. Dutta, V. M. Shalaev, and A. Boltasseva, Photonic spin Hall effect in robust phase gradient metasurfaces utilizing transition metal nitrides, ACS Photonics **6**, 99 (2019).

[38] S. Li, X. Li, G. Wang, S. Liu, L. Zhang, C. Zeng, L. Wang, Q. Sun, W. Zhao, and W. Zhang, Multimensional manipulation of photonic spin Hall effect with a single-layer dielectric metasurface, Adv. Opt. Mater. **7**, 1801365 (2019).

[39] M. R. Akram, X. Bai, R. Jin, G. A. E. Vandenbosch, M. Premaratne, and W. Zhu, Photonic spin Hall effect-based ultra-thin transmissive metasurface for efficient generation of OAM waves, IEEE Trans. Antenn. Propag. **67**, 4650 (2019).

[40] M. Kim, D. Lee, Y. Yang, Y. Kim, and J. Rho, Reaching the highest efficiency of spin Hall effect of light in the near-infrared using all-dielectric metasurfaces, Nat. Commun. **13**, 2036 (2022).

[41] W. Chen, Y. Liu, and B. Guo, Tunable modulation of photonic spin Hall effect owing to the defect mode in one-dimensional photonic crystal with plasma, Phys. Plasmas **26**, 052110 (2019).

[42] Y. Wang, T. Tang, Y. Mao, R. Wang, F. Li, C. Li, and J. Shen, Spin Hall effect of tunnelling mode in one-dimensional photonic crystal based on frustrated total internal reflection, Superlattice Microstruct. **143**, 106542 (2020).

[43] J. Xia, Y. Chen, and Y. Xiang, Enhanced spin Hall effect due to the redshift gaps of photonic hypercrystals, Opt. Express **29**, 12160 (2021).
[44] H. Da, Q. Song, and H. Ye, Directional dependent magnetooptical effect and the photonic spin Hall effect in a magnetic Weyl semimetal-based photonic crystal, Opt. Lett. **47**, 4359 (2022).
[45] Y. Xiang, X. Jiang, Q. You, J. Guo, and X. Dai, Enhanced spin Hall effect of reflected light with guided-wave surface plasmon resonance, Photonics Res. **5**, 467 (2017).
[46] Z. Chen, W. Zhen, H. Xu, G. Zhuang, Z. Zhang, H. Zhang, X. Zhang, and Y. Meng, Giant longitudinal spin Hall effect for elliptically polarized light under surface plasmon resonance, J. Opt. **25**, 025401 (2023).
[47] W. J. M. Kort-Kamp, F. J. Culchac, R. B. Capaz, and F. A. Pinheiro, Photonic spin Hall effect in bilayer graphene moiré superlattices, Phys. Rev. B **98**, 195431 (2018).
[48] M. Cheng, P. Fu, X. Tang, S. Chen, X. Chen, Y. Lin, and S. Fang, Tunable and enhanced spin Hall effect of light in layered nanostructures containing graphene, J. Opt. Soc. Am. B **35**, 1829 (2018).
[49] X.-G. Luo, M.-B. Pu, X. Li, and X.-L. Ma, Broadband spin Hall effect of light in single nanoapertures, Light Sci. Appl. **6**, e16276 (2017).
[50] A. P. Slobozhanyuk, A. N. Poddubny. I. S. Sinev, A. K. Samusev, Y. F. Yu, A. I. Kuznetsov, A. E. Miroshnichenko, and Y. S. Kivshar, Enhanced photonic spin Hall effect with subwavelength topological edge states, Laser Photonics Rev. **10**, 656 (2016).
[51] P. V. Kapitanova, P. Ginzburg, F. J. Rodríguez-Fortuño, D. S. Filonov, P. M. Voroshilov, P. A. Belov, A. N. Poddubny, Y. S. Kivshar, G. A. Wurtz, and A. V. Zayats, Photonic spin Hall effect in hyperbolic metamaterials for polarization-controlled routing of subwavelength modes, Nat. Commun. **5**, 3226 (2014).
[52] O. Takayama, J. Sukham, R. Malureanu, A. V. Lavrinenko, and G. Puentes, Photonic spin Hall effect in hyperbolic metamaterials at visible wavelengths, Opt. Lett. **43**, 4602 (2018).
[53] H. Chen, S. Zhou, G. Rui, and Q. Zhan, Magnified photonic spin-Hall effect with curved hyperbolic metamaterials, J. Appl. Phys. **124**, 233104 (2018).
[54] C. W. Hsu, B. Zhen, A. D. Stone, J. D. Joannopoulos, and M. Soljačić, Bound state in the continuum, Nat. Rev. Mater. **1**, 16048 (2016).
[55] A. A. Bogdanov, K. L. Koshelev, P. V. Kapitanova, M. V. Rybin, S. A. Gladyshev, Z. F. Sadrieva, K. B. Samusev, Y. S. Kivshar, and M. F. Limonov, Bound states in the continuum and Fano resonances in the strong mode coupling regime, Adv. Photonics **1**, 016001 (2019).
[56] S. Joseph, S. Pandey, S. Sarkar, and J. Joseph, Bound states in the continuum in resonant nanostructures: An overview of engineered materials for tailored applications, Nanophotonics **10**, 4175 (2021).
[57] A. F. Sadreev, Interference traps waves in an open system: Bound states in the continuum, Rep. Prog. Phys. **84**, 055901 (2021).
[58] E. N. Bulgakov and A. F. Sadreev, Bound states in the continuum in photonic waveguides inspired by defects, Phys. Rev. B **78**, 075105 (2008).
[59] Y. Plotnik, O. Peleg, F. Dreisow, M. Heinrich, S. Nolte, A. Szameit, and M. Segev, Experimental Observation of Optical Bound States in the Continuum, Phys. Rev. Lett. **107**, 183901 (2011).
[60] N. M. Shubin, V. V. Kapaev, and A. A. Gorbatsevich, Multimode resonances, intermode bound states, and bound states in the continuum in waveguides, Phys. Rev. B **106**, 125425 (2022).
[61] K. Koshelev, S. Lepeshov, M. Liu, A. Bogdanov, and Y. Kivshar, Asymmetric Metasurfaces with High-$Q$ Resonances Governed by Bound States in the Continuum, Phys. Rev. Lett. **121**, 193903 (2018).
[62] S. Xiao, M. Qin, J. Duan, F. Wu, and T. Liu, Polarization-controlled dynamically switchable high-harmonic generation from all-dielectric metasurfaces governed by dual bound states in the continuum, Phys. Rev. B **105**, 195440 (2022).
[63] C. W. Hsu, B. Zhen, J. Lee, S. Chua, S. G. Johnson, J. D. Joannopoulos, and M. Soljačić, Observation of trapped light within the radiation continuum, Nature (London) **499**, 188 (2013).
[64] Y. Yang, C. Peng, Y. Liang, Z. Li, and S. Noda, Analytical Perspective for Bound States in the Continuum in Photonic Crystal Slabs, Phys. Rev. Lett. **113**, 037401 (2014).
[65] J. Jin, X. Yin, L. Ni, M. Soljačić, B. Zhen, and C. Peng, Topologically enabled ultrahigh-$Q$ guided resonances robust to out-of-plane scattering, Nature (London) **574**, 501 (2019).
[66] C. Zhao, W. Chen, J. Wei, W. Deng, Y. Yan, Y. Zhang, and C.-W. Qiu, Electrically tunable and robust bound states in the continuum enabled by 2D transition metal dichalcogenide, Adv. Opt. Mater. **10**, 2201634 (2022).
[67] P. Hu, J. Wang, Q. Jiang, J. Wang, L. Shi, D. Han, Z. Q. Zhang, C. T. Chan, and J. Zi, Global phase diagram of bound states in the continuum, Optica **9**, 1353 (2022).
[68] D. C. Marinica and A. G. Borisov, Bound States in the Continuum in Photonics, Phys. Rev. Lett. **100**, 183902 (2008).
[69] H. M. Doeleman, F. Monticone, W. den Hollander, A. Alù, and A. F. Koenderink, Experimental observation of a polarization vortex at an optical bound state in the continuum, Nat. Photonics **12**, 397 (2018).
[70] W. Zhang, A. Charous, M. Nagai, D. M. Mittleman, and R. Mendis, Extraordinary optical reflection resonances and bound states in the continuum from a periodic array of thin metal plates, Opt. Express **26**, 13195 (2018).
[71] R. Kikkawa, M. Nishida, and Y. Kadoya, Polarization-based branch selection of bound states in the continuum in dielectric waveguide modes anti-crossed by a metal grating, New J. Phys. **21**, 113020 (2019).
[72] F. Wu, J. Wu, Z. Guo, H. Jiang, Y. Sun, Y. Li, J. Ren, and H. Chen, Giant Enhancement of the Goos-Hänchen Shift Assisted by Quasibound States in the Continuum, Phys. Rev. Appl. **12**, 014028 (2019).
[73] T. Ning, X. Li, Y. Zhao, L. Yin, Y. Huo, L. Zhao, and Q. Yue, Giant enhancement of harmonic generation in all-dielectric resonant waveguide gratings of quasibound states in the continuum, Opt. Express **28**, 34024 (2020).
[74] F. Wu, M. Luo, J. Wu, C. Fan, X. Qi, Y. Jian, D. Liu, S. Xiao, G. Chen, H. Jiang, Y. Sun, and H. Chen, Dual quasi-bound states in the continuum in compound grating waveguide structures for large positive and negative Goos-Hänchen shifts with perfect reflection, Phys. Rev. A **104**, 023518 (2021).
[75] I. A. M. A.-Ani, K. As'Ham, L. Huang, A. E. Miroshnichenko, and H. T. Hattori, Enhanced strong coupling of TMDC

monolayers by bound state in the continuum, Laser Photonics Rev. **15**, 2100240 (2021).
[76] F. Wu, C. Fan, K. Zhu, J. Wu, X. Qi, Y. Sun, S. Xiao, H. Jiang, and H. Chen, Tailoring electromagnetic responses in a coupled-grating system with combined modulation of near-field and far-field couplings, Phys. Rev. B **105**, 245417 (2022).
[77] C. Shi, J. Hu, X. Liu, J. Liang, J. Zhao, H. Han, and Q. Zhu, Double-layer symmetric gratings with bound states in the continuum for dual-band high-*Q* optical sensing, Beilstein J. Nanotechnol. **13**, 1408 (2022).
[78] E. N. Bulgakov and A. F. Sadreev, Self-trapping of nanoparticles by bound states in the continuum, Phys. Rev. B **106**, 165430 (2022).
[79] X. Jiang, J. Tang, Z. Li, Y. Liao, L. Jiang, X. Dai, and Y. Xiang, Enhancement of photonic spin Hall effect via bound states in the continuum, J. Phys. D: Appl. Phys. **52**, 045401 (2019).
[80] Y. Yang, K. Kelley, E. Sachet, S. Campione, T. S. Luk, J.-P. Maria, M. B. Sinclair, and I. Brener, Femtosecond optical polarization switching using a cadmium oxide-based perfect absorber, Nat. Photonics **11**, 390 (2017).
[81] J. Wang, L. Shi, and J. Zi, Spin Hall Effect of Light Via Momentum-Space Topological Vortices around Bound States in the Continuum, Phys. Rev. Lett. **129**, 236101 (2022).
[82] M. F. Al-Kuhaili, Optical properties of hafnium oxide thin films and their applications in energy-efficient windows, Opt. Mater. **27**, 383 (2004).
[83] E. Palik, *Handbook of Optical Constants of Solids I* (Academic Press, New York, 1985).
[84] T. Sang, S. Cai, and Z. Wang, Guided-mode resonance filter with an antireflective surface consisting of a buffer layer with refractive index equal to that of the grating, J. Mod. Opt. **58**, 1260 (2011).
[85] A. Yariv and P. Yeh, *Optical Waves in Crystals* (Wiley, New York, 1984).
[86] M. G. Moharam, D. A. Pommet, E. B. Grann, and T. K. Gaylord, Stable implementation of the rigorous coupled-wave analysis for surface-relief gratings: Enhanced transmittance matrix approach, J. Opt. Soc. Am. A **12**, 1077 (1995).
[87] F. Li, Use of Fourier series in the analysis of discontinuous periodic structures, J. Opt. Soc. Am. A **13**, 1870 (1996).
[88] Y. Zhang, W. Liu, Z. Li, Z. Li, H. Cheng, S. Chen, and J. Tian, High-quality-factor multiple Fano resonances for refractive index sensing, Opt. Lett. **43**, 1842 (2018).
[89] H. Luo, X. Ling, X. Zhu, W. Shu, S. Wen, and D. Fan, Enhancing or suppressing the spin Hall effect of light in layered nanostructures, Phys. Rev. A **84**, 033801 (2011).
[90] M. Kim, D. Lee, B. Ko, and J. Rho, Diffraction-induced enhancement of optical spin Hall effect in a dielectric grating, APL Photonics **5**, 066106 (2020).
[91] Y. Wan, Z. Zheng, W. Kong, X. Zhao, Y. Liu, Y. Bian, and J. Liu, Nearly three orders of magnitude enhancement of Goos-Hanchen shift by exciting Bloch surface wave, Opt. Express **20**, 8998 (2012).
[92] J. M. Khoshman and M. E. Kordesch, Optical properties of a-$HfO_2$ thin films, Surf. Coat. Technol. **201**, 3530 (2006).
[93] L. Wang, H. Liu, Y. Jiang, X. Yang, D. Liu, Y. Ji, F. Zhang, and D. Chen, Effects of hot-isostatic pressing and anneling post-treatment on $HfO_2$ and $Ta_2O_5$ films prepared by ion beam sputtering, Optik **142**, 33 (2017).
[94] Z. S. Liu, S. Tibuleac, D. Shin, P. P. Young, and R. Magnusson, High-efficiency guided-mode resonance filter, Opt. Lett. **23**, 1556 (1998).
[95] Z. Liu, Y. Xu, Y. Lin, J. Xiang, T. Feng, Q. Cao, J. Li, S. Lan, and J. Liu, High-*Q* Quasibound States in the Continuum for Nonlinear Metasurfaces, Phys. Rev. Lett. **123**, 253901 (2019).